ROYAL SOCIETY
OF CHEMISTRY

Check for updates

NIR-responsive porous gold nanorod dispersed in a 3D gelatin scaffold for stimulus-responsive drug release and synergistic therapy†

Snigdharani Panda,[a] Irfan Khan,[a] Suditi Neekhra,[b] Rohit Srivastava[b] and
Sunita Srivastava ID *[a]

Biodegradable porous nanomaterials have emerged as a promising avenue for tumor drug delivery owing to their capacity to encapsulate large quantities of drugs and their compatibility with biological systems. Despite the widespread recognition of gold nanorods for their therapeutic potential, studies on porous gold nanorods remain relatively few. Herein, we synthesized thiol-functionalized porous gold nanorods (PGNRs) that exhibit strong absorbance in the NIR region of light spectrum (750 nm), resulting in excellent photothermal properties with a photothermal conversion efficiency of 79%. Meanwhile, the intrinsic porous structure with a multimodal pore size and large surface area of 261 m^2 g^{-1} makes PGNR an ideal material for different drug carriers. A model drug doxorubicin loaded on PGNR with 98.7% encapsulation efficiency exhibits good cationic Au and π interaction and a large surface area. To prevent premature drug release and ensure sustained drug delivery at the target site, we designed gelatin and tannic acid-based thermoresponsive hydrogels capturing PGNR-DOX in the matrix. Upon exposure to an NIR laser of 750 nm wavelength, the temperature of this hydrogel increased beyond the upper critical solution temperature (42 °C), leading to a gel-to-sol phase transition that enhances PGNR-DOX release at the specific site. This NIR-triggered hyperthermia facilitates tumor penetration, and the drug conjugate quickly dissociated in an intrinsic acidic environment due to weak cation–π interaction. The effects of phototherapy and chemotherapy together are demonstrated through *in vitro* experiments. Therefore, this NIR light-responsive nanoplatform holds promising properties and can be considered an ideal material for *in vivo* studies.

1. Introduction

Noble metals such as Au, Ag, and Pt conjugated with drug carriers that can respond to various exogenous stimuli such as H$_2$O$_2$,[1] light,[2] temperature,[3] pH,[4] and electric field[5] have recently gained significant attention owing to their extensive use in overcoming current pathological hurdles. These stimulus-responsive nanomaterials have the following advantages: (i) they can minimize drug dosage and maximize therapeutic efficiency; (ii) they can circulate in the bloodstream for a long time without stimuli; (iii) external stimulus-controlled release occurs at a target specific site; and (iv) permeability and retention factor can be enhanced *via* tuning the size, shape,

composition and functionality of the drug delivery system. At present, owing to their inherent unique features, such as low toxicity, bactericidal activity, tunable optical resonance in the NIR region, excellent hydrophilicity, ease of surface functionality, and flexible aspect ratio, anisotropic gold nanostructures have emerged as protagonists in the field of science and technology.[6] Thus far, most anisotropic gold nanostructures have a CTAB surfactant coating, which introduces toxicity and limits surface group availability.[7] Therefore, the conjugation of drug molecules on a solid nanorod surface is slightly complicated. In comparison to solid gold nanostructures, porous nanostructures have been employed as the most efficient multimodal nanostructures with a large surface area, distinctive size tunable optical and physical properties and greater ability to accumulate high drug dosage.[8] Few porous nanostructures such as hollow carbon, silica, and copper spheres have been reported for biomedical and energy purposes.[9,10] The keen interest in porous gold nanorods as biomedical agents stems from their advantages, including dispersibility in water, increased surface area, structural defects, interesting optical

[a] *Soft Matter and Nanomaterials Laboratory, Department of Physics, Indian Institute of Technology Bombay, Powai, Mumbai 400076, India.*
E-mail: sunita.srivastava@iitb.ac.in

[b] *Nanobios Lab, Department of Bioscience and Bioengineering, Indian Institute of Technology Bombay, Powai, Mumbai 400076, India*

† Electronic supplementary information (ESI) available. See DOI: https://doi.org/10.1039/d4ma00400k

properties, and thermal conductivity. However, reports on hollow and porous gold nanorods for multimodal therapy are few. Recently, Kai et al. reported the synthesis of amino acid-coated hollow gold nanorods with significant absorbance in the NIR-II region, which made this material a demanding agent for photothermal as well as photoacoustic imaging.[11] Theoretical and experimental studies illustrate that both NIR I (700–1000 nm) and short NIR II (1000–1150 nm) show better deep tissue penetration compared to the UV-vis spectrum and that longer wavelength radiation reduces the scattering from biological tissue components significantly.[12] Thorough investigation of the penetration capability of laser in depth revealed that short NIR-II shows the best results for kidney, spleen and liver while NIR I suitably works for muscle, stomach, heart and brain tissues.[13] Although nanomaterial has many advantages, direct cellular uptake of nanomaterial can impose toxicity to plasma membranes because of their reactive surface. For example, the interaction of positively charged nanomaterials with negatively charged cell membranes can lead to the disruption of the continuum of cell membranes.[14] Afterwards, polymer-functionalized nanomaterials, such as PEGylated gold nanoparticles, are used for drug delivery systems. These interactions with proteins show conformational changes that may lead to neurodegenerative diseases.[15] To overcome this tricky situation nowadays, liposomes and biocompatible hydrogels have emerged as good carriers of nanomaterials and drug molecules. Interestingly, hydrogels comprising biologically active moieties, such as collagen, gelatin and elastin, support cell growth, migration, and proliferation.[16] 3D crosslinking scaffolds can adopt nanomaterial and drug molecules inside their network structure and can be released at targeted places under specific physiological conditions.[17] Gelatin-derived hydrogels are nontoxic and biocompatible and generally mimic the innate arginine–glycine–asparagine sequence chemically and structurally; over time, they can be easily degradable using matrix metalloproteinase enzyme. Only gelatin-derived hydrogels are stable at 29-33 °C.[18] Addition of a crosslinking agent can enhance its mechanical strength through hydrogen and covalent bonding.[19] In continuation with the above findings, herein, we fabricated a 2-aminothiol ethane functionalized porous gold nanorod (PGNR) and its porous surface carrying doxorubicin model drug through hydrophobic-π interaction. This nanodrug (PGNR-DOX) showed optimum absorbance at 750 nm wavelength (which falls on the NIR-I region). To achieve targeted and controlled drug release, this nanodrug was implanted within gelatin and tannic acid-based thermo-responsive hydrogel. On 750 nm of NIR laser exposer, PGNR induced heat and attained phase transition temperature inside the gel. This facilitated the stimuli-responsive release of PGNR-DOX at the targeted area (Scheme 1). We expect that there would be multiple benefits to using this novel hydrogel formulation; easy penetration in cell membrane, external light responsive PGNR-DOX release, pH-based stimuli at local area, high photothermal conversion efficiency of PGNR, and thermal images can provide information about the exact location of cancerous cells. The detailed investigation on structure and functionality, drug release profile, photothermal behavior, and gelation network were studied in detail.
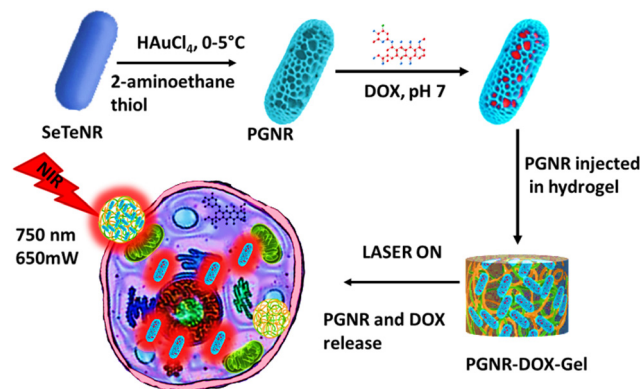
Scheme 1 Schematic representation of the synthesis of PGNR, gel encapsulation, and NIR light-triggered therapeutic action.

2. Experimental section

2.1 Chemicals and reagents

All the chemicals used in synthesis, characterization and application are listed below. Selenous acid (H_2SeO_3), tellurium dioxide (TeO_2), hydrazine monohydrate ($NH_2–NH_2\cdot H_2O$), tetra chloroauric (III) acid hydrate ($HAuCl_4$), 2-aminoethane thiol, doxorubicin hydrochloride, gelatin-A (from porcine skin) and tannic acid were procured from Sigma-Aldrich. Sodium dodecyl sulphate (SDS), resazurin sodium salt and DAPI were supplied by MERCK chemicals. Ultrapure deionized water collected from the Merck Milli-pore system (resistivity 18.2 MΩ cm) was further autoclaved and then used for both synthesis and experiments. Dulbecco's Modified Eagle's Media (DMEM), trypsin-EDTA solution (0.25% trypsin and 0.02% EDTA in DPBS), fetal bovine serum (FBS), Dulbecco's phosphate-buffer saline (DPBS), and antibiotic antimycotic solution (10 000 units of penicillin, 10.0 mg of streptomycin and 25 μg of amphotericin B per mL in 0.9% normal saline) were purchased from HiMedia, India. Paraformaldehyde was purchased from Otto Chemie Pvt. Ltd, India. Mouse fibroblast (L929) and cervical cancer (HeLa) cell lines, obtained from NCCS, India, were cultured in a complete DMEM medium under standard conditions of 37 °C and 5% CO_2. Complete DMEM includes 10% (v/v) fetal bovine serum and 1% (v/v) antibiotic–antimycotic solution.

2.2 Synthesis of porous gold nanorod

The synthesis of porous gold nanorod (PGNR) was performed using galvanic replacement of Se_xTe_y nanorod in the presence of $HAuCl_4$ and cysteamine.[20] The Se_xTe_y NR template was synthesized in an aqueous medium by the in situ reduction of selenous acid and tellurium dioxide mixture through excess treatment with hydrazine hydrate:[21]

$$x H_2SeO_3 + y TeO_2 + N_2H_4\cdot H_2O \rightarrow Se_xTe_y\,(\downarrow) + N_2\,(\uparrow) + H_2O.$$
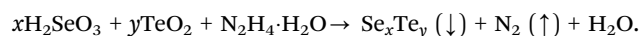
Here, the catalytic amount of Se (0.3 mL, 5.4 mM) was chosen with Te (0.016 g) and 8 mL hydrazine monohydrate precursor to obtain a nanorod with consistent aspect size and volume, as shown in Fig. S1 (ESI†). Further, the addition of chloroauric acid creates electrochemical driving forces,

facilitating the replacement of Se–Te elements with Au ions through the following reaction:

$$AuCl_4^- + Te(Se) + H_2O \rightarrow Au + (TeO_3)^{2-} + (SeO_3)^{2-} + Cl^- + H^+.$$
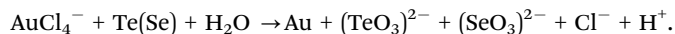
An 80 mL, 3 μM solution of 2-aminoethanethiol was pre-cooled in a reagent bottle at 5 °C for 45 minutes, followed by the addition of 10 mL of selenium telluride rods and stirring for 15 minutes. Subsequently, 1.2 mL of HAuCl₄ solution at 25 mM was slowly added to this mixture and left stirring for 10 minutes, resulting in the formation of PGNR. Cysteamine-functionalized PGNRs were centrifuged twice at 890 × g for 5 minutes to remove excess surfactant. The pellets were then collected and dispersed in aqueous media for further experimentation.

2.3 Structure and surface characterization

10 μL of diluted aqueous samples (Se–Te NR template and PGNR) were deposited on a freshly piranha-cleaned silicon substrate and vacuum-dried until the solvent was evaporated. Further, FEG-SEM images were collected using a JEOL JSM-7600F microscope at 10 kV. Similarly, a TEM grid of 3 mm diameter and a 200 mesh-sized carbon-coated copper grid were used to image the PGNR sample using the FEG-TEM 200 kV facility. Analyses of particle size and its Gaussian size distribution were performed by considering 50 individual nanorods obtained from FEG-TEM images using ImageJ software. A Malvern Zeta Sizer (ZS-90) equipped with a folded capillary zeta potential cell (DTS-1070) was used to measure the surface charge of the above samples. The zeta potential values are reported as the average of three independent measurements of each sample. Surface functional groups on the nanorod sample and elemental composition of the PGNR sample were evaluated using an FTIR spectrophotometer, Bruker and electron spectroscopy for chemical analysis instruments (ESCA, Kratos analytical, AXIS Supra). Small-angle X-ray scattering (Xeuss 2.0, Xenocs) of the template and PGNR samples were measured using 50 μL of samples in a thin capillary tube to evaluate roughness and porosity on the surface. A BET surface area analyser (Quanta chrome) was employed with the N₂ adsorption–desorption method at 120 °C degassing temperature for 12 h to investigate the porous surface area and pore diameter of the PGNR sample.

2.4 Doxorubicin loading and quantification

The absorbance spectra of the nanorods were measured using a Jasco V-730 UV-vis spectrophotometer to quantify drug loading and monitor drug release. The doxorubicin (DOX) drug molecules are loaded into the porous cavity of PGNR using the nanoprecipitation protocol.[22] Typically, an aqueous solution of 5 mg (1 mg mL⁻¹) of PGNR was incubated with DOX (0.5 mg mL⁻¹) in a vial for 48 hours. The drug loading capacity of PGNR was monitored through absorbance obtained from the supernatant (∼488 nm) at different time intervals using a UV-vis spectrophotometer. Drug encapsulation and loading efficiency can be calculated as follows:

$$\text{Drug encapsulation efficiency} = \frac{W_{\text{total drug}} - W_{\text{free drug}}}{W_{\text{total drug}}} \times 100,$$

$$\text{Drug loading (\%)} = \frac{W_{\text{total drug}} - W_{\text{free drug}}}{W_{\text{PGNR}}} \times 100.$$

2.5 Photothermal property of PGNR

The absorption spectra of freshly synthesized PGNR particles exhibit strong absorption peaks in the NIR-I region, as shown in Fig. 3a. To evaluate the photothermal response, PGNR samples were irradiated with a high-power diode laser (750 nm wavelength) at fixed power densities (1 W cm⁻²) for 20 minutes. The nanoparticle solutions in quartz cuvettes at varying concentrations (50, 150, and 300 μg mL⁻¹) were positioned 5 cm from the laser source. PGNR during the laser irradiation digital thermocouple is used to monitor the solution temperature at 30-second intervals for 15 minutes until the temperature reaches an equilibrium value. Photothermal conversion efficiency, η of the sample is calculated using the formula[23]

$$\eta = \frac{hA(T_{\text{max}} - T_{\text{sur}}) - Q_{\text{dis}}}{I(1 - 10^{-A\lambda})},$$

where η is the photothermal conversion efficiency, h is the heat transfer coefficient, and A is the area of the container. The estimate of $hA = \frac{mC_p}{\tau_s}$, where m is the mass of the sample solution, C_p is specific heat capacity, and τ_s is the linear slope of ln θ vs. cooling time plot. θ is the ratio of $(T_{\text{amb}} - T_{\text{surr}})$ to $(T_{\text{max}} - T_{\text{surr}})$. Q_{dis} is thermal loss due to natural convection, I is incident laser power and A is the absorbance under the 750 nm laser.

2.6 PGNR-DOX dispersion in gelatin–tannic acid hydrogel matrix (PGNR-DOX-Gel)

A homogenous hydrogel was prepared by mixing 5 wt% of each porcine skin gelatin (type A), tannic acid and 1 mg mL⁻¹ of PGNR in Milli-Q water. The mixture was stirred at 40 °C for 1 hour, followed by a gradual temperature increase (1 °C min⁻¹) until a uniform solution was obtained. The prepared hydrogel solution was swiftly injected into custom-designed silicon molds (diameter 2 cm, thickness 1 cm). The pre-gel solution was then refrigerated at 4 °C for 24 hours and stored under a vacuum for future use. For comparison, a control hydrogel (Ge–Ta) was prepared using the same method but without the addition of PGNR.

2.7 Rheological measurements

The rheological properties of neat and PGNR-incorporated hydrogels were investigated to estimate their temperature dependence melting and elastic response using Rheometer TA HR30 with a cone-plate of 20 mm diameter with a cone angle of 1°. Before testing, the samples were loaded onto the rheometer stage and sealed with silicon oil to prevent solvent evaporation. Measurements were conducted on hydrogels aged

for 1 and 7 days. A strain of 1% was identified from the amplitude sweep measurement to ensure the linear viscoelastic response of the samples. Frequency sweep measurements were conducted from 10 Hz to 0.1 Hz at a constant temperature of 25 °C. Additionally, a temperature sweep experiment was performed from 25 °C to 60 °C at a fixed frequency of 10 Hz and a strain of 0.01%.

2.8 Drug release sensitivity to external stimuli of pH and light

Drug release triggered by external stimuli, such as pH variation and exposure to light, offers a sophisticated approach to targeted drug delivery. To evaluate the pH-dependent release of drug molecules from PGNRs, a standardized protocol was followed. Typically, 1 mg of PGNRs was dispersed in 4 mL of distinct pH solutions (4.1, 5.2, 6.2, and 7.3) within separate vials, followed by incubation at 37 °C for 2 days. To quantify drug release over time, the supernatant from each vial was collected at predetermined intervals and analysed using UV-vis absorbance spectroscopy for the measurement of specific drug concentrations based on their characteristic absorbance wavelengths. Further, the PGNR-DOX-gel sample was subjected to a series of NIR laser exposure cycles to investigate its drug release behaviour. A 750 nm laser was applied for 5 minutes, followed by a 5-minute pause, and this cycle was continuously repeated for a total of 100 minutes. The drug release profile from the hydrogel was then monitored and analysed.

2.9 *In vitro* evaluation of biocompatibility and cytotoxicity

The biocompatibility of three hydrogels (neat, PGNR-gel and PGNR-DOX-gel) was assessed using a colorimetric AlamarBlue to evaluate their impact on cell viability.[24] Mouse fibroblast L929 cells were cultured in complete DMEM and were harvested by trypsinization for seeding in the well plate. Approximately 8000 cells per well were seeded onto a 96-well plate and incubated for 24 hours to allow for adherence and growth. Subsequently, varying concentrations of the aforementioned materials were added to separate wells and incubated for another 24 hours to assess their potential impact on cell viability. For the positive control, 1% Triton X-100 was used, and for the negative control, complete DMEM media was used. After 24 h of exposure to the material, the cells in each well of a 96-well plate were washed twice with PBS buffer and incubated with Resazurin sodium salt (10 μg well) for 4 hours. Using a Tecan Infinite M200 Pro Plate reader, we measured the intensity of a fluorescent signal emitted by the cells (excitation/emission wavelengths: 560/590 nm), which indicated their viability. The estimate of cell viability was obtained using the following equation:

$$\text{Cell viability (\%)} = \frac{\text{Emission intensity of sample}}{\text{Emission intensity of negative control}} \times 100.$$

The above-mentioned PGNR, PGNR-DOX-Gel and free DOX were used to treat HeLa cell lines, and cytotoxicity was measured under laser OFF and ON condition (750 nm, 650 mW) following the above-mentioned protocol.

2.10 Apoptosis imaging

HeLa cancer cell lines were seeded into two 6-well plates with a cell density of 6000 cells per well and cultured overnight at 37 °C. The seeded cells were treated with media, neat, PGNR-gel and PGNR-DOX-gel (100 μg mL^{-1} of each sample) and left for the encapsulation of particles. The NIR continuous laser source was exposed for 5 minutes to one of the post-encapsulated 6-well plates (750 nm, 1.0 W) that was left for 24 h of incubation. The other plate is left for incubation under dark conditions for the same time duration. Thereafter, all the cell nuclei were stained with 4′,6-diamidino-2-phenylindole (1 μg mL^{-1}) for 15 minutes under dark conditions, centrifuged, washed, and then subjected to imaging using laser scanning confocal microscopy (Carl Zeiss, LSM-780 model).

2.11 Statistical analysis

Drug release and *in vitro* studies were expressed as mean values ± standard deviations of at least 3 independent experiments. One-way analysis of variance (ANOVA) test, followed by *post hoc* analyses (Tukey), was performed using Graph Pad Prism software to compare the treatment groups. $P < 0.05$ was considered statistically significant for all the analyses.

3. Results and discussion

3.1 Morphology and surface modification of PGNR

In Fig. 1, we showed the structural characterization data (SEM and TEM images) for the size and shape estimate of the freshly prepared PGNR sample. The formation of well-defined anisotropic nanorods with fairly monodisperse sizes is depicted in Fig. 1a. The size distribution analysis after taking an average of a large number of PGNRs revealed average length and diameter estimates to be 180 ± 20 nm and 80 ± 20 nm, respectively. As shown in Fig. 1b, the PGNR rods have an aspect ratio of ∼2. The high-resolution TEM images illustrated in Fig. 1c reveal a porous structure on the surface of the gold nanorod and asymmetric holes within its crystalline structure. These features are likely due to the Kirkendall effect.[25] High-resolution TEM and SAED (selected area electron diffraction) analysis reveal a lattice spacing of 0.23 nm, which is consistent with the (111) plane of face-centered cubic Au (inset Fig. 1c).

Further, zeta potential measurements and Fourier-transform infrared (FTIR) spectroscopy (Fig. S2 and S3, ESI†) reveal significant differences in the surface chemistry of the template and PGNRs. The presence of sodium dodecyl sulfate (SDS) adsorbed on the SeTe NR template results in a negative surface charge of approximately −39.5 mV. In contrast, the porous nanorods exhibit a positive surface charge of approximately +25 mV.

This suggests a stronger Au–S bond facilitated by the 2-amino thiophenol, which likely promotes a galvanic reaction, leading to the observed positive charge. As shown in Fig. S3 (ESI†), FTIR spectra emphasized O–H stretching frequency near 3400 cm^{-1}, −CH$_2$ stretching frequencies at 2850 and 2910 cm^{-1}, and peaks at 1300–1600 cm^{-1} corresponding to S=O and N–O stretching frequencies. However, on PGNR formation, a strong peak at 700–800 cm^{-1} region confirmed the presence of the metal–sulphide (Au–S) group. Free NH$_2$ group was also evidenced from both N–H stretching and
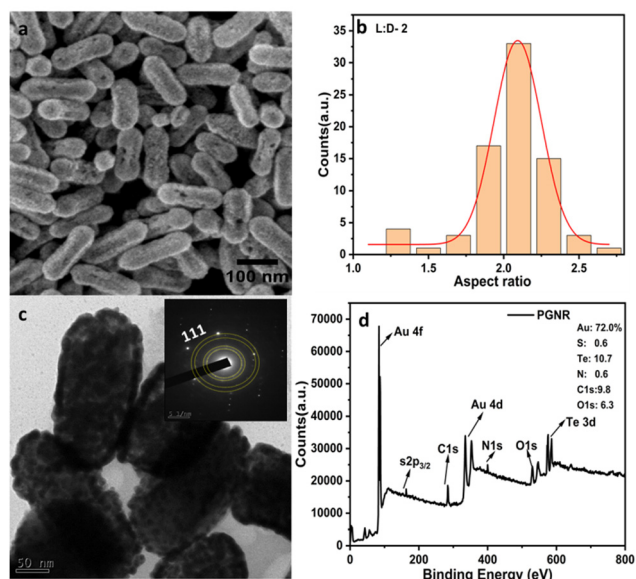
Fig. 1 (a) FESEM image of PGNR, (b) size distribution curve of the L : D ratio of PGNR. (c) HRTEM image of PGNR and its corresponding SAED pattern. (d) XPS survey spectrum of PGNR sample showing binding energies of Au (4f/4d), S (2p), C (1s), N (1s), O (1s), Te (3d) electrons.

bending frequency at 3400 cm^{-1} and 1100 cm^{-1}, respectively. Further, the XPS survey spectrum of PGNR displayed in Fig. 1d reveals prominent surface binding energies at 83–89 eV, 337–355 eV, 162 eV, 284.1 eV, 400 eV, 531 eV, and 575–586 eV corresponding to Au 4f, Au 4d, S 2p, C 1s, N 1s, O 1s and Te 3d with mass percentages of 72.0 (Au 4f/4d), 0.6, 9.8, 6.3 and 10.6%, respectively. High-resolution spectra of Au displayed two significant peaks at 83.8 and 87.5 eV, which can be correlated to 4f$_{7/2}$ and 4f$_{5/2}$ binding energies, proving gold atoms are strongly bonded to the surface of the material (Fig. S4, ESI†).

3.2 Porosity and surface fractal of PGNR

The morphology study shown in Fig. 1 reveals a surface asymmetric and the formation of a porous structure. To further quantify the features of the surface, heterogeneity analysed surface fractal geometry using two complementary techniques: N$_2$ adsorption–desorption isotherm and X-ray scattering methods. The adsorption–desorption measurements shown in Fig. 2a indicate a type-IV isotherm for PGNR with a high surface area of 261 m^2 g^{-1}. The pore size distribution on the nanorod surface was found to be multimodal. The particle exhibited small pores with narrow size distributions of 4.5 nm and 6.0 nm, likely at the outer layer. Additionally, broader pores around 26 nm were attributed to the inner core. In Fig. 2b, we present the scattering profile, $I(q)$ vs. q from the SAXS measurements to unravel the length scale-dependent heterogeneity in the sample. The scattering intensity is fitted to a cylindrical model using Sasview software. The fitted data in the low q range (0.005–0.007 Å^{-1}) resulted in slopes of −4.0, −3.37 and −3.7 for the template, PGNR and PGNR-DOX, respectively. Although a theoretically smooth nanoscale particle would scatter with a slope of −4, as observed in the nanorod template, we measured deviations from this expected
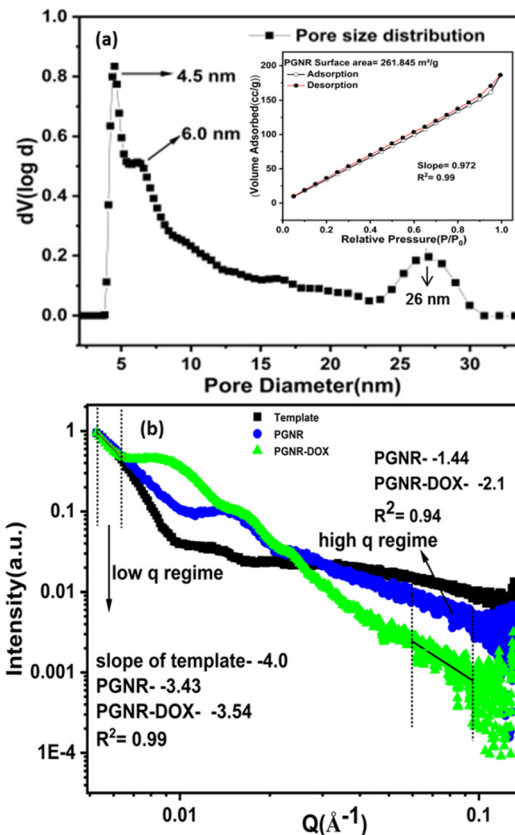

Fig. 2 (a) Multimodal pore size distribution of PGNR; inset: N$_2$ adsorption–desorption isotherm of PGNR and (b) SAXS line profile of the template, PGNR and PGNR-DOX.

slope with values of −3.4 (PGNR) and −3.7 (PGNR-DOX). This suggests the presence of a diffuse surface boundary layer.[26] Analysis of scattering data in the high q range revealed details about the surface properties. The exponents derived from the linear region of the data (−1.4 for PGNR and −2.1 for PGNR-DOX) were used to calculate the surface fractal dimensions using the equation $s = 2d - D_s$, where s is the slope, d is the Euclidean dimension (2 for surfaces), and D_s is the surface fractal value.[27]

The estimates of $D_s \sim 2.6$ for PGNR and 1.9 for PGNR-DOX suggest a more irregular and rough surface for the PGNR sample compared to PGNR-DOX. This observation is consistent with the results obtained from the data in Fig. S5 (ESI†) using the Frenkel–Halsey–Hill (FHH) equation for multilayer gas adsorption mentioned below.[28]

$$\ln(\text{volume adsorbed}) = s[\ln(P_0/P)] + \text{const.}$$

A linear fit to the above equation (shown in Fig. S5, ESI†) results in a slope of −0.98 and $R^2 = 0.99$ for the PGNR sample. This slope (s) was used to evaluate the surface fractal (D) of the nanorod using the formula $s = D - 3$. From the BET multipoint graph, the surface fractal value was calculated to be 2.02 for the PAuNR, which also supports the SAXS data, proving the irregularity and surface roughness of the PGNR.

3.3 Photothermal properties

Gold nanorods are attractive photothermal agents due to their ability to tune the surface plasmon resonance peak in the near-infrared (NIR) region. To gain further insight into the optical properties of these specific porous gold nanorods, we employed UV-vis spectroscopy. As shown in Fig. S6 (ESI†), SeTe nanorods absorb light at 340 nm due to the n–π* transition of the metal ions. Interestingly, upon transformation into the porous gold structure (Fig. S6, ESI†), a broad surface plasmon resonance band emerges in the visible-near infrared regime (λ_{max} = 750 nm). This newly acquired near-infrared (NIR-I) absorption opens exciting possibilities for exploring the photothermal applications of these nanorods. Template and PGNR samples display distinct grey and blue colors (Fig. S6 inset, ESI†) due to spectral variations in scattering and absorption, respectively.

Fig. 3a depicts the temperature changes observed during the photothermal studies of the PGNR samples at various concentrations. 50 µg mL^{-1} of the PGNR sample exhibits a temperature increase from 27 °C to 35.7 °C within 10 minutes of continuous laser irradiation, reaching saturation at 15 minutes. Higher concentrations (100 and 300 µg mL^{-1}) show proportionally higher equilibrium temperatures of 41 °C and 54 °C, respectively, under identical conditions. This observation suggests an increase in sample temperature depending on the PGNR concentration in the solution. Deionized water as control exhibits no significant change in temperature, while the template, at the highest measured concentration ($\sim$300 µg mL^{-1}) displayed a marginal increase in temperature of 12 °C only. To assess the reusability of the PGNR material, we evaluated the photothermal stability of PGNR and PGNR-DOX-Gel by subjecting them to three cycles of laser irradiation (ON), followed by

deactivation (OFF), as shown in Fig. S10 (ESI†). The materials maintained their effectiveness throughout these cycles, demonstrating good reusability for multiple laser treatments. Fig. 3b demonstrates PGNR's exceptional photothermal performance. The cooling curve exhibits a linear relationship between cooling time and the natural log of temperature difference, $(-\ln(\theta))$, yielding a time constant of $\approx$420.03 seconds. Furthermore, the calculated photothermal conversion efficiency is 79.25%, outperforming most existing NIR-I/II-based hollow nanostructures (Table S1, ESI†).[11,29–34] In Fig. 3c, we present thermal images captured at various time intervals during irradiation on 300 µg mL^{-1} PGNR solution with a 750 nm laser (1 W) for 10 minutes. The thermal maps of the samples indicate a uniform temperature increase in the region of the samples close to the laser irradiation. It can be observed that with an increase in the time interval, the temperature increases and finally reaches equilibrium after 15 minutes. These results demonstrate that PGNR is an excellent photothermal candidate.

3.4 DOX loading and release

The drug loading and its release properties of PGNR are presented in Fig. 4a. The absorbance of the supernatant (at 488 nm), a signature of DOX concentration, decreased significantly over time, confirming successful drug encapsulation on the porous PGNR surface. As evidenced from the literature, the aromatic ring of DOX exhibits good interaction with cationic gold nanostructure and is expected to be absorbed in the porous structure of PGNR to facilitate encapsulation.[35] The PGNR synthesized here exhibits an excellent drug encapsulation efficiency of $\sim$98%, which is comparable to some of the best drug carriers reported in Table S2 (ESI†).[36–46] For this system, we estimate that the amount of drug loaded per unit mass of the nanocarrier is $\sim$10%. This result indicates that even though we have excellent drug encapsulation efficiency, the drug loading per particle/PGNR can be improved in the future.

In Fig. 4b, we show the pH-dependent stability of the loaded drug on the PGNR. Drug release was found to depend on the time and the pH of the environment. The rate of drug release was found to increase with time at all pH levels. We find that drug release is more stable at high pH (6 and 7); however, lowering pH environments (pH 4 and 5) triggered faster release, with around 20–25% of DOX release after 40 hours (Fig. 4b). The triggered drug release in an acidic environment might be due to the complete ionization of DOX molecules, which reduces their hydrophobicity and promotes desorption from the PGNR surface. The estimate of the time-dependent cumulative drug release shown in Fig. 4b was derived from UV-vis absorption data at various pH levels (Fig. S7, ESI†). For all malignant cell studies, these nanocarriers are subjected to an intrinsic acidic pH environment, and we incorporate the PGNR-DOX system within the gelatin–tannic acid-based hydrogel. This hydrogel exhibits thermoresponsive behavior for controlled and stimuli-based drug release.[47,48]

Interestingly, porous gold nanorods offer significantly greater advantages than solid gold nanorods in terms of cargo loading and photothermal efficiency. We performed a thorough
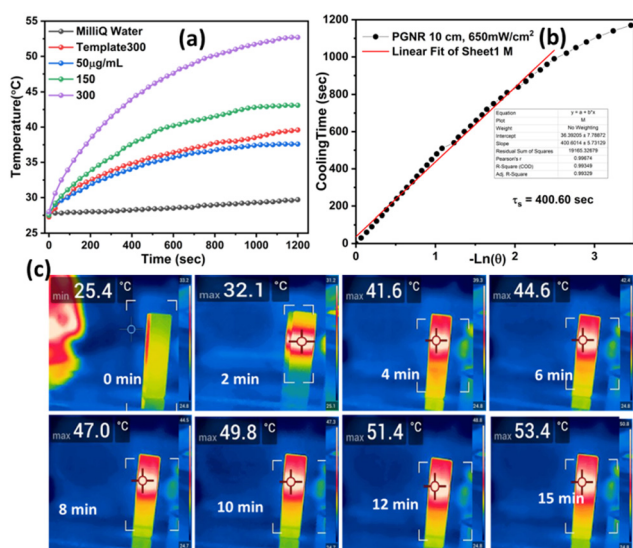

Fig. 3 (a) Elevation of temperature of aqueous dispersion of different concentrations of PGNR upon 20 minutes continuous 750 nm laser exposure. (b) Cooling time vs. negative ln(θ), where θ is derived from temperature difference gained from solution (300 µg mL^{-1}) as mentioned in (a). (c) IR thermal image of 300 µg mL^{-1} PGNR sample at different time gaps during laser irradiation.
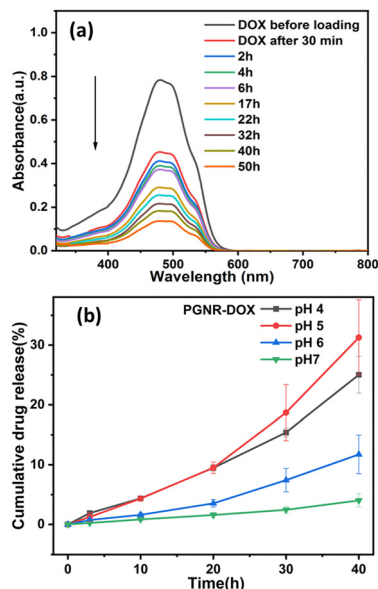
Fig. 4   (a) DOX loading on the porous matrix of PGNR is observed using a UV-vis spectrophotometer and (b) release of DOX from PGNR-DOX in response to pH stimuli.

Fig. 5   (a) Amplitude sweep test with strain variation (0.1–1000%) of Ge–Ta and PGNR-DOX-gel at 1 rad s^{-1} frequency. (b) Temperature sweep test of the Ge–Ta and PGNR-DOX-gel hydrogel at 1 rad s^{-1} frequency and 10% strain, (c) quantification of the swelling percentage of Ge–Ta and PGNR-DOX-gel hydrogel at pH 7 and pH 5, and (d) DOX release at intracellular pH with 750 nm laser irradiation (5 minutes ON–OFF cycle) from PGNR-DOX particle and PGNR-DOX-gel.

literature survey, comparing the performance of porous *vs.* solid nanorods (for the same dimension of rods), and the existing studies unravel significantly smaller photothermal conversion efficiency for solid nanorods.[49] Studies by R. Wang *et al.*, have shown that the photothermal conversion efficiency of solid gold nanorods (of length ∼100 nm similar to our PGNR system) exhibits an efficiency of 51%,[50] measured using an 809 nm laser at 1.72 W. Excitingly, our porous nanorods, with comparable size, exhibit (∼79%) significantly higher photothermal efficiency. The performance of porous gold nanorods reported in this work is analyzed through SAXS, BET and drug loading efficiency measurements. Additionally, the high surface area in porous gold nanorod systems allows them to carry larger amounts of cargo.

3.5   Photothermal behavior of stimuli (temperature and pH) responsive hydrogel

The thermoresponsive properties of the PGNR sample dispersed in Ge–Ta hydrogel are measured by performing viscoelastic studies using a TA 30 rheometer. First, an amplitude sweep test was carried out by subjecting the hydrogels (Ge–Ta hydrogel, PGNR-DOX-gel) to variable strains ranging from 0.1 to 1000% to identify the linear viscoelastic region. As shown in Fig. 5a, both the storage modulus (G') and loss modulus (G'') exhibit constant values at oscillation strains in the range of ∼0.1–40%, indicating a linear viscoelastic regime. Therefore, a strain of 10% within this linear regime was chosen for all subsequent dynamic measurements.

Frequency sweep measurements at various temperatures were conducted to determine the gel's melting point by evaluating the crossover of the elastic modulus and loss modulus (Fig. 5b). The gel-melting temperatures for the Ge–Ta hydrogel and PGNR-DOX-gel were observed to be 33.0 °C and 42.3 °C,
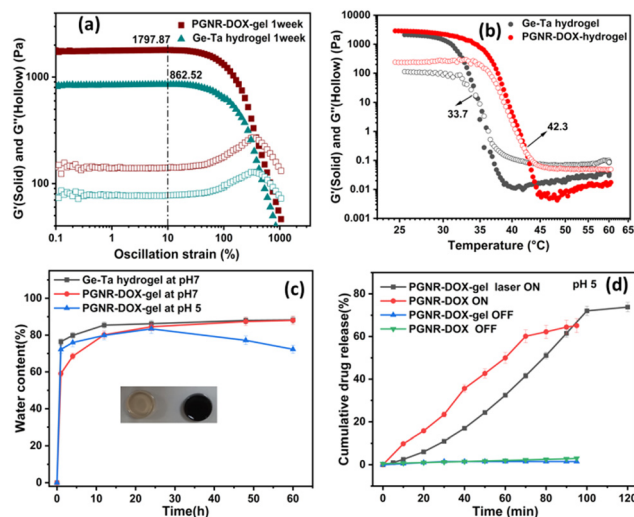
respectively. The gel phase exhibited dominant elastic characteristics with $G' > G''$. However, upon transition to the sol phase, this behavior flips, indicating a viscous liquid-like state with $G' < G''$. The temperature-responsive phase transition suggests the potential for controlled drug release by manipulating the gel's phase transition.

Further, the pH-responsive swelling and stability of PGNR-DOX-gel were investigated under neutral (pH 7) and mildly acidic (pH 5) conditions. The PGNR-DOX-gel exhibited rapid swelling, reaching a plateau within 12 hours and maintaining minimal further changes for up to 60 hours (Fig. 5c). However, under acidic conditions, these hydrogels showed signs of degradation after 24 hours. This degradation is likely attributed to a reduction in crosslinking density due to the increased protonation of amino groups in the acidic environment.[51] Prolonged exposure to acidic conditions can compromise the gel stability, leading to the rapid release of particles under external stimuli of pH.

The photothermal response of suspended PGNR-DOX and PGNR-DOX encapsulated in the hydrogel is shown in Fig. 5d under Laser ON and OFF conditions. The cumulative drug release data is recorded for ∼1.5 hours for all the samples. For the laser ON conditions, the sample was exposed to NIR light for ∼5 minutes. As shown in Fig. 5d, under light OFF conditions (for 5 minutes), we estimate less drug release (1%) for nanocarriers encapsulated in the hydrogel, whereas for the suspended sample, we measure ∼3% of drug release. These data suggest that hydrogel incorporation is useful in controlling intrinsic drug release. The laser ON condition results in a significantly large dosage of drug release, which can be controlled by monitoring the number of exposure cycles to the sample. Fig. S8 (ESI†) presents detailed results on the statistical

significance of differences between the laser ON and laser OFF conditions for each group shown in Fig. 5d. The laser exposure increases the internal temperature of the material, prompting gel–sol phase transition. Additionally, the acidic environment weakens the cation–π interaction between DOX and Au. These two combined effects result in the promotion of rapid drug release. We find that repeated increases in sample exposure result in an increase in the drug release with time, as shown in Fig. 5d. For the PGNR system, we measured ∼72% of drug release with 7 cycles of LASER ON exposure for 5 minutes. Thus, we show that PGNR-DOX embedded in hydrogel has the potential for controlled and triggered drug release applications. The laser exposure cycle provides control, and the thermoresponsive behavior of the hydrogel is useful for triggering drug release. Thus, PGNR-DOX hydrogel samples have the potential for combinatorial therapies.

3.6 Biocompatibility and cytotoxicity study

The biocompatibility and cytotoxicity behaviour of Ge–Ta hydrogel, PGNR-gel and PGNR-DOX-gel were tested on L929 and HeLa cells, at varying concentrations in the range from 10–150 μg mL^{-1} for 24 hours. The cell viability estimates are always ≫ 50% for Ge–Ta, PGNR-gel and PGNR-DOX-gel, suggesting that these materials have negligible reverse effects on healthy cells under LASER-OFF conditions. We observed that cell viability decreases with an increase in the concentration of Ge–Ta hydrogel, PGNR-gel and PGNR-DOX-gel and the maximum effect on cell viability was found for PGNR-DOX-gel. However, these effects are not significant as we estimated that even at very high concentrations of the material (∼150 μg mL^{-1}), the cell viability was ∼65% for PGNR-DOX-gel treated cells. Ge–Ta hydrogel-treated cells were minimally affected in terms of their cell viability, and their response was very similar to that of the control sample. Therefore, under LASER OFF conditions, estimates of cell viability are ≫50% for all the samples.

Under laser irradiation (Laser ON), PGNR-DOX-gels treated with L929 cells demonstrated a dose-dependent response (Fig. 6a). Up to a concentration of 100 μg mL^{-1}, cell viability remained above 50% (IC50 value). However, higher concentrations of the material significantly decreased cell viability. This suggests that a maximum dosage of 100 μg mL^{-1} of PGNR-DOX-gel material is safe and suitable for *in vitro* studies. Thus, all the colorimetric assays for cytotoxicity evaluation were performed at varying material concentrations of up to 100 μg mL^{-1}.

The AlamarBlue assay in HeLa cells under both laser OFF and ON conditions is shown in Fig. 6b. For free DOX, we reach an IC50 value at material concentrations > 20 μg mL^{-1}; however, the reported literature evidenced that 13 μg mL^{-1} of DOX is enough to achieve significant IC50 against HeLa cells.[52] At a maximum concentration of ∼100 μg mL^{-1} of free DOX, we find that almost all the Hela cells are dead, suggesting ∼0% cell viability. Further, on the incubation of HeLa cells with PGNR and PGNR-DOX-gel, we measured approximately 82% and 75% of cells that remained viable, respectively, under laser off conditions. Thus, we conclude that both the PGNR-hydrogel
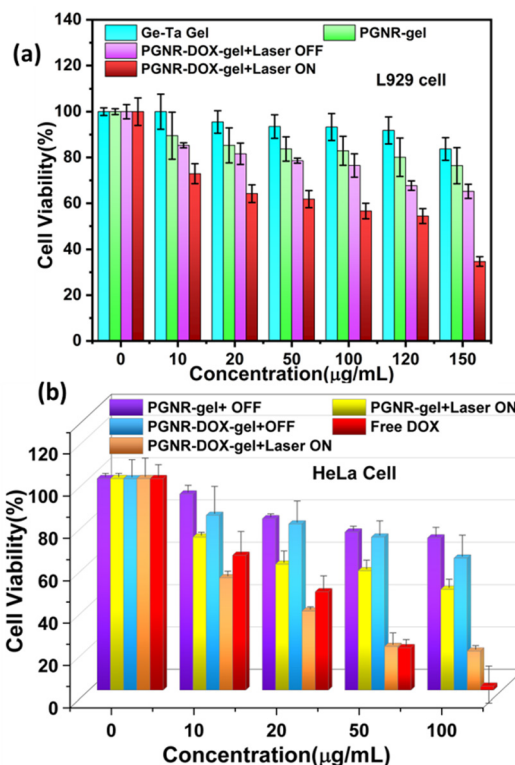

Fig. 6 (a) Biocompatibility assay of L929 cells after treatment with (0, 10, 20, 50, 100, 120, and 150 μg) concentrations of the Ge–Ta hydrogel, PGNR-gel and PGNR-DOX-gel for 24 h. (b) Viability of HeLa cell line post-incubation with (0, 10, 20, 50, and 100 μg) concentrations of the Ge–Ta hydrogel, PGNR-gel and PGNR-DOX-gel in the absence and presence of 5 minutes, 750 nm laser irradiation (650 mW cm^{-2} at 5 cm height).

and PGNR-DOX-hydrogel exhibit minimal cytotoxicity effects on cell viability under laser OFF conditions. Interestingly, laser irradiation for 5 minutes (750 nm 650 mW cm^{-2}) showed remarkable acute toxic effects, and cell viability declined to 60% and 25% for PGNR-gel and PGNR-DOX-gel samples, respectively (Fig. 6b). The difference in cell viability for both L929 and HeLa cells under laser ON and OFF conditions is statistically depicted in Fig. S9a and b (ESI†), respectively.

These data suggest that even PGNR-gel has a strong cell-killing ability through photothermal phenomena. The significantly large decrease in cell viability for PGNR-DOX-gel compared to PGNR-gel can be explained as the local temperature increases due to the strong absorption of PGNR dispersed in a gel matrix. Gel–sol phase transition of thermo responsive hydrogel facilitates hyperthermia and PGNR-DOX release. A significant drop in cell viability is induced by the controlled release of doxorubicin in response to external stimuli. This, combined with the intrinsic acidic pH environment of Hela cells due to malignancy, offers the high performance of our sample.

To summarize, our study demonstrates that 50% growth inhibition of HeLa cells can be achieved using 20 μg of PGNR-DOX-gel, 100 μg of PGNR material, or 20 μg of free doxorubicin (Table S2, ESI†). Hence, we conclude that the combinatorial therapeutic material leads to less usage of direct chemo drugs
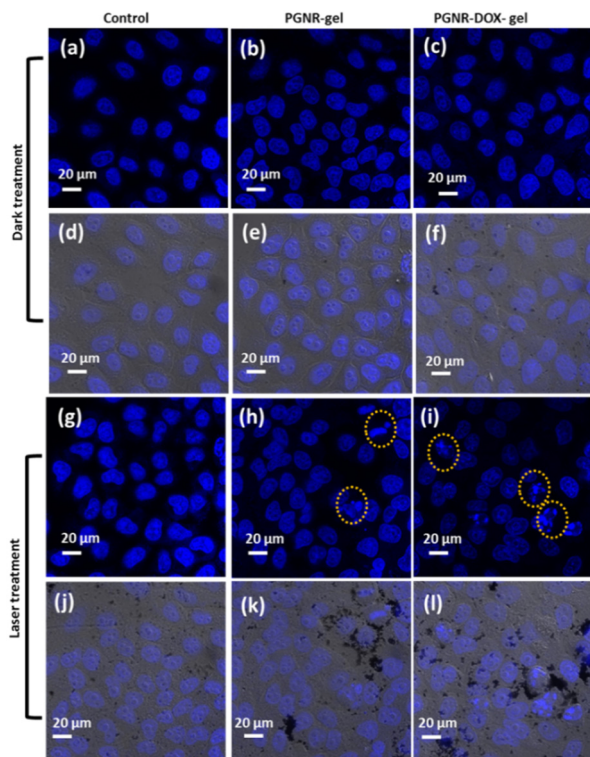
Fig. 7 Confocal images of DAPI-stained HeLa cell lines in the dark and laser treatment for 5 minutes under 750 nm. Control: (a), (d), (g), and (j), PGNR-gel treated: (b), (e), (h), and (k), and PGNR-DOX-gel: (c), (f), (i), and (l).

and high efficiency of photo and chemo therapy together compared to individual photo and chemotherapy.

3.8 Confocal imaging

The real-time confocal images of HeLa cells treated with PGNR-gel and PGNR-DOX-gel are shown in Fig. 7 (under laser on and off conditions) to visualize the cytotoxicity effects. It can be observed from the DAPI-stained nuclei that exposure to laser light on HeLa cells does not affect cell viability. The images in Fig. 7a and d and Fig. 7g and j show that Hela cells exhibit healthy nuclei under both the laser OFF and ON conditions, respectively. For the laser OFF condition, no notable morphological changes were detected for the HeLa cells treated with PGNR (b) and (e) or PGNR-DOX-gels (c) and (f). With Laser On, the HeLa cells displayed evidence of nuclear rupture compared to the control groups. Further, it can be observed that the nuclei rupture concentration increases for PGNR-DOX-gels and laser On. These results are consistent with the observation from the cytotoxicity measurements shown in Fig. 6b. Bright field images of the cytoplasmic state of each treatment in Fig. 7 are represented separately in Fig. S11 (ESI†).

An analysis of multiple laser scanning confocal image frames revealed a clear distinction in cell death rates between the groups (control, PGNR, and PGNR-DOX-Gel under laser OFF and ON) in Fig. 8. Notably, the control group, regardless of laser activation (ON or OFF), exhibited negligible apoptosis. In contrast, HeLa cells treated with PGNR and PGNR-DOX-gel under laser irradiation (ON condition) displayed significant cell death, reaching 15% and 27% in each confocal image frame, respectively. The statistical significance
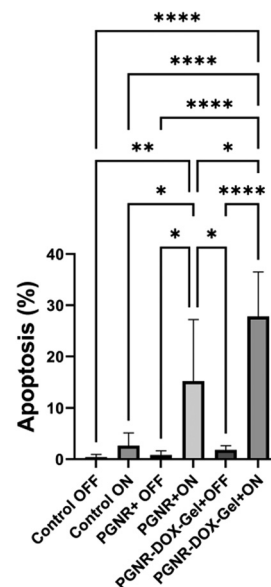

Fig. 8 Quantification of apoptosis rate from multiple confocal image frames using automated cell counting in ImageJ software.

was calculated with a one-way ANOVA test with alpha 0.05, $*p$ is 0.021, $**p$ is 0.0094 and $****p$ is <0.0001. These findings suggest that the combined photothermal and chemotherapeutic approaches *via* cytoplasmic treatment effectively stimulate nucleoplasm activity, potentially leading to the elimination of malignant cells.

Conclusion

We successfully synthesized cysteamine-functionalized gold nanorods (PGNRs) using a galvanic replacement method. A detailed characterization of size and surface chemistry was performed to obtain uniform homogeneous nanoparticle dispersions. The porous nanorods possess a uniform aspect ratio of ~ 2, a high surface area (261 m^2 g^{-1}), and multimodal pores (4.5 nm, 6 nm, and 26 nm). Interestingly, PGNRs exhibit an exceptional photothermal efficiency of 79%, which is the highest reported for porous materials to date, making them promising candidates for drug delivery and photothermal therapy applications. Further, the presence of porous surfaces allows for loading capability. The PGNR samples exhibit an excellent drug encapsulation efficiency of $\sim 99\%$. Further, PGNR-DOX is successfully entrapped inside thermo-responsive Ge–Ta hydrogel for controlled DOX release in response to NIR light and intracellular pH. *In vitro* experiments demonstrate that DOX-loaded hydrogel effectively kills the HeLa cell line *via* synergistic photo and chemotherapy. The high photothermal conversion efficiency, porosity, and biocompatibility of PGNR make it a promising material for sensing and biomedical applications.

Author contributions

S. Panda and I. Khan has contributed to synthesis, characterization, and property study of the material. S. Panda performed

data analysis and manuscript writing. S. Neekhra has performed *in vitro* cell experiments under the guidance of R. Srivastava. S. Srivastava has secured funding, supervised project, contributed to data analysis and manuscript writing.

Conflicts of interest

There are no conflicts to declare.

Acknowledgements

References

1 S. K. Maji, *ACS Appl. Nano Mater.*, 2019, **2**, 7162–7169.
2 Y. Tao, H. F. Chan, B. Shi, M. Li and K. W. Leong, *Adv. Funct. Mater.*, 2020, **30**, 2005029.
3 M. Karimi, P. Sahandi Zangabad, A. Ghasemi, M. Amiri, M. Bahrami, H. Malekzad, H. Ghahramanzadeh Asl, Z. Mahdieh, M. Bozorgomid and A. Ghasemi, *ACS Appl. Mater. Interfaces*, 2016, **8**, 21107–21133.
4 L. Liu, Y.-X. Liu, H. Zhong, X.-R. Li, Y.-L. Jun, Q.-L. Wang, L.-S. Ding, Z.-P. Cheng and H.-Y. Qian, *Colloids Surf., B*, 2023, **229**, 113432.
5 Z. Zhang, X. Yang, Y. Zhao, F. Ye and L. Shang, *Adv. Mater.*, 2023, **35**, 2300220.
6 K. Ghanem, Y. Li, J. Xu and C. Kan, *Phys. Chem. Chem. Phys.*, 2023, **25**, 18545–18576.
7 N. Timmer, D. Gore, D. Sanders, T. Gouin and S. T. Droge, *Chemosphere*, 2019, **222**, 461–468.
8 Z. Su and T. Chen, *Small*, 2021, **17**, 2005354.
9 B. Zhao, J. Fu, C. Zhou, L. Yu and M. Qiu, *Small*, 2023, **19**, 2301917.
10 K.-W. Kim, J. Kim, C. Jo and J. K. Kim, *J. Mater. Chem. A*, 2023, **11**, 7358–7386.
11 K. Cai, W. Zhang, M. F. Foda, X. Li, J. Zhang, Y. Zhong, H. Liang, H. Li, H. Han and T. Zhai, *Small*, 2020, **16**, 2002748.
12 J. Zhao, D. Zhong and S. Zhou, *J. Mater. Chem. B*, 2018, **6**, 349–365.
13 A. Sun, H. Guo, Q. Gan, L. Yang, Q. Liu and L. Xi, *Opt. Express*, 2020, **28**, 9002–9013.
14 Ü. Anık, S. Timur and Z. Dursun, *Int. J. Polym. Mater. Polym. Biomater.*, 2020, **69**, 1090–1100.
15 T. Aghaie, M. H. Jazayeri, M. Manian, L. Khani, M. Erfani, M. Rezayi, G. A. Ferns and A. Avan, *J. Cell. Biochem.*, 2019, **120**, 2749–2755.
16 P. Lavrador, M. R. Esteves, V. M. Gaspar and J. F. Mano, *Adv. Funct. Mater.*, 2021, **31**, 2005941.
17 Z. Sun, C. Song, C. Wang, Y. Hu and J. Wu, *Mol. Pharmaceutics*, 2019, **17**, 373–391.
18 R. Andreazza, A. Morales, S. Pieniz and J. Labidi, *Polymers*, 2023, **15**, 1026.
19 S. Zafar, M. Hanif, M. Azeem, K. Mahmood and S. A. Gondal, *Polym. Bull.*, 2022, **79**, 9199–9219.
20 H. Cheng, C. Wang, D. Qin and Y. Xia, *Acc. Chem. Res.*, 2023, **56**, 900–909.
21 W. Zhang, K. Cai, X. Li, J. Zhang, Z. Ma, M. F. Foda, Y. Mu, X. Dai and H. Han, *Theranostics*, 2019, **9**, 4971.
22 Y. Liu, G. Yang, D. Zou, Y. Hui, K. Nigam, A. P. Middelberg and C.-X. Zhao, *Ind. Eng. Chem. Res.*, 2019, **59**, 4134–4149.
23 X. Liu, B. Li, F. Fu, K. Xu, R. Zou, Q. Wang, B. Zhang, Z. Chen and J. Hu, *Dalton Trans.*, 2014, **43**, 11709–11715.
24 E. M. Longhin, N. El Yamani, E. Rundén-Pran and M. Dusinska, *Front. Toxicol.*, 2022, **4**, 981701.
25 D. Thiry, L. Molina-Luna, E. Gautron, N. Stephant, A. Chauvin, K. Du, J. Ding, C.-H. Choi, P.-Y. Tessier and A.-A. El Mel, *Chem. Mater.*, 2015, **27**, 6374–6384.
26 C. Raschpichler, C. Goroncy, B. Langer, E. Antonsson, B. Wassermann, C. Graf, P. Klack, T. Lischke and E. Rühl, *J. Phys. Chem. C*, 2020, **124**, 16663–16674.
27 A. Y. Cherny, E. M. Anitas, V. A. Osipov and A. I. Kuklin, *Phys. Chem. Chem. Phys.*, 2019, **21**, 12748–12762.
28 T. Ren, Y. Si, J. Yang, B. Ding, X. Yang, F. Hong and J. Yu, *J. Mater. Chem.*, 2012, **22**, 15919–15927.
29 Y. Qing, S. Qi, Y. Meng, W. Jinping, W. Siyu, L. Li, C. Yu, W. Yidan, S. Yilin, T. Fengping and N. Li, *ACS Appl. Mater. Interfaces*, 2017, **9**, 40017–40030.
30 L. Ao, C. Wu, K. Liu, W. Wang, L. Fang, L. Huang and W. Su, *ACS Appl. Mater. Interfaces*, 2018, **10**, 12544–12552.
31 S. Li, L. Zhang, X. Liang, T. Wang, X. Chen, C. Liu, L. Li and C. Wang, *Chem. Eng. J.*, 2019, **378**, 122175.
32 S. Lin, H. Chen, R. Wang, T. Jiang and F. Yu, *Biomater. Sci.*, 2023, **11**, 4874–4889.
33 Y. Chen, W. Meng, M. Chen, L. Zhang, M. Chen, X. Chen, J. Peng, N. Huang, W. Zhang and J. Chen, *J. Mater. Chem. B*, 2023, **11**, 10003–10018.
34 Q. Gao, X. He, L. He, J. Lin, L. Wang, Y. Xie, A. Wu and J. Li, *Nanoscale*, 2023, **15**, 17987–17995.
35 S. Palvai, D. Kpeglo, G. E. Newham, S. A. Peyman, S. D. Evans and Z. Y. Ong, *ACS Appl. Mater. Interfaces*, 2024, **16**, 5568–5581.
36 S. R. Bhosale, R. R. Bhosale, R. P. Dhavale, G. B. Kolekar, V. B. Shimpale and P. V. Anbhule, *Langmuir*, 2024, **40**, 6471–6483.
37 A. Gupta, A. Sood, D. Bhardwaj, N. Shrimali, R. Singhmar, S. Chaturvedi, P. Guchhait and G. Agrawal, *Adv. Therap*, 2024, **7**, 2300165.
38 Z. Li, T. Kovshova, J. Malinovskaya, P. Valikhov, P. Melnikov, N. Osipova, O. Maksimenko, N. Dhakal, A. Chernysheva, V. Chekhonin, S. Gelperina and M. G. Wacker, *Small*, 2023, 2306726.
39 U. Patel, K. Rathnayake, N. Singh and E. C. Hunt, *ACS Appl. Bio Mater.*, 2023, **6**, 1915–1933.

40 L. Li, Y. Yang, Y. Lv, P. Yin and T. Lei, *Colloids Surf., B*, 2020, **186**, 110720.

41 Y. Zou, D. Li, Y. Wang, Z. Ouyang, Y. Peng, H. Tomás, J. Xia, J. Rodrigues, M. Shen and X. Shi, *Bioconjugate Chem.*, 2020, **31**, 907–915.

42 P. Wei, Y. Li, Y. Wu, Y. Zhang, Y. Xiang and J. Chen, *J. Mater. Chem. B*, 2024, **12**, 3521–3532.

43 T. Cui, J. Liang, H. Chen, D. D. Geng, L. Jiao, J. Y. Yang, H. Qian, C. Zhang and Y. Ding, *ACS Appl. Mater. Interfaces*, 2017, **9**, 8569–8580.

44 M. Hasani, S. Jafari, H. A. Javar, H. Abdollahi and H. Rashidzadeh, *ACS Appl. Bio Mater.*, 2023, **6**, 1019–1031.

45 J. Lin, H. Yang, Y. Zhang, F. Zou, H. He, W. Xie, Z. Zou, R. Liu, Q. Xu, J. Zhang, G. Zhong, Y. Li, Z. F. Tang, Y. Deng, S. Cai, L. Wang, Y. Huang, Y. Zhuo, X. Jiang and W. Zhong, *Small*, 2023, **19**, 2205024.

46 T. Wang, X. Zhang, Y. Pan, X. Miao, Z. Su, C. Wang and X. Li, *Dalton Trans.*, 2011, **40**, 9789–9794.

47 D. Curry, A. Cameron, B. MacDonald, C. Nganou, H. Scheller, J. Marsh, S. Beale, M. Lu, Z. Shan and R. Kaliaperumal, *Nanoscale*, 2015, **7**, 19611–19619.

48 P. Gheysoori, A. Paydayesh, M. Jafari and H. Peidayesh, *Eur. Polym. J.*, 2023, **186**, 111846.

49 J. W. Xiao, S. X. Fan, F. Wang, L. D. Sun, X. Y. Zheng and C. H. Yan, *Nanoscale*, 2014, **6**, 4345–4351.

50 H. Chen, L. Shao, T. Ming, Z. Sun, C. Zhao, B. Yang and J. Wang, *Small*, 2010, **6**(20), 2272–2280.

51 C. Chen, H. Yang, X. Yang and Q. Ma, *RSC Adv.*, 2022, **12**, 7689–7711.

52 D. Hemalatha, M. Suneetha, H. Kim, U. T. Uthappa, K. S. V. Krishna Rao and S. S. Han, *Colloids Surf., A*, 2024, **682**, 132879.